

# Towards human SuperEEG

Lucy L. W. Owen<sup>1</sup>, Andrew C. Heusser<sup>1,2</sup>, and Jeremy R. Manning<sup>1\*</sup>

<sup>1</sup>Department of Psychological and Brain Sciences, Dartmouth College,  
Hanover, NH 03755, USA

<sup>2</sup>Akili Interactive,  
Boston, MA 02110, USA

## Abstract

Human *SuperEEG*<sup>1</sup> entails measuring ongoing neural activity throughout the entire living brain with perfect precision and arbitrarily high spatiotemporal resolution. Although true SuperEEG is impossible using existing methods, here we present a model-based method for *inferring* full-brain neural activity at millimeter-scale spatial resolutions and millisecond-scale temporal resolutions using standard human intracranial recordings. Our approach assumes that different people's brains exhibit similar spatial correlations, and that activity and correlation patterns are spatially smooth. One can then ask, for an arbitrary individual's brain: given recordings from a limited set of locations in that individual's brain, along with the observed spatial correlations learned from other people's recordings, how much can be inferred about ongoing activity at *other* locations in that individual's brain?

**Keywords:** Electrocorticography (ECoG), intracranial electroencephalography (iEEG), local field potential (LFP), epilepsy, maximum likelihood estimation, Gaussian process regression

## Introduction

Modern human brain recording techniques are fraught with compromise [33]. Commonly used approaches include functional magnetic resonance imaging (fMRI), scalp electroencephalography (EEG), and magnetoencephalography (MEG). For each of these techniques, neuroscientists and electrophysiologists must choose to optimize spatial resolution at the cost of temporal resolution (e.g., as in fMRI) or temporal resolution at the cost of spatial resolution (e.g., as in EEG and MEG). A less widely used approach (due to requiring work with neurosurgical patients) is to record from electrodes implanted directly onto the cortical surface (electrocorticography; ECoG)

---

<sup>1</sup>The term "SuperEEG" was coined by Robert J. Sawyer in his popular science fiction novel *The Terminal Experiment* [29]

25 or into deep brain structures (intracranial EEG; iEEG). However, these intracranial approaches  
26 also require compromise: the high spatiotemporal resolution of intracranial recordings comes  
27 at the cost of substantially reduced brain coverage, since safety considerations limit the number  
28 of electrodes one may implant in a given patient’s brain. Further, the locations of implanted  
29 electrodes are determined by clinical, rather than research, needs.

30 An increasingly popular approach is to improve the effective spatial resolution of MEG or  
31 scalp EEG data by using a geometric approach called *beamforming* to solve the biomagnetic or  
32 bioelectrical inverse problem [28]. This approach entails using detailed brain conductance mod-  
33 els (often informed by high spatial resolution anatomical MRI images) along with the known  
34 sensor placements (localized precisely in 3D space) to reconstruct brain signals originating from  
35 theoretical point sources deep in the brain (and far from the sensors). Traditional beamforming  
36 approaches must overcome two obstacles. First, the inverse problem beamforming seeks to  
37 solve has infinitely many solutions. Researchers have made traction towards constraining the  
38 solution space by assuming that signal-generating sources are localized on a regularly spaced  
39 grid spanning the brain and that individual sources are small relative to their distances to the  
40 sensors [1, 11, 34]. The second, and in some ways much more serious, obstacle is that the  
41 magnetic fields produced by external (noise) sources are substantially stronger than those pro-  
42 duced by the neuronal changes being sought (i.e., at deep structures, as measured by sensors  
43 at the scalp). This means that obtaining adequate signal quality often requires averaging the  
44 measured responses over tens to hundreds of responses or trials (e.g., see review by [11]).

45 Another approach to obtaining high spatiotemporal resolution neural data has been to col-  
46 lect fMRI and EEG data simultaneously. Simultaneous fMRI-EEG has the potential to balance  
47 the high spatial resolution of fMRI with the high temporal resolution of scalp EEG, thereby,  
48 in theory, providing the best of both worlds. In practice, however, the signal quality of both  
49 recordings suffers substantially when the two techniques are applied simultaneously (e.g., see

50 review by [13]). In addition, the experimental designs that are ideally suited to each technique  
51 individually are somewhat at odds. For example, fMRI experiments often lock stimulus presen-  
52 tation events to the regularly spaced image acquisition time (TR), which maximizes the number  
53 of post-stimulus samples. By contrast, EEG experiments typically employ jittered stimulus pre-  
54 sentation times to maximize the experimentalist’s ability to distinguish electrical brain activity  
55 from external noise sources such as from 60 Hz alternating current power sources.

56 The current “gold standard” for precisely localizing signals and sampling at high temporal  
57 resolution is to take (ECoG or iEEG) recordings from implanted electrodes (but from a limited  
58 set of locations in any given brain). This begs the following question: what can we infer about  
59 the activity exhibited by the rest of a person’s brain, given what we learn from the limited  
60 intracranial recordings we have from their brain and additional recordings taken from *other*  
61 people’s brains? Here we develop an approach, which we call *SuperEEG*, based on Gaussian  
62 process regression [27]. SuperEEG entails using data from multiple people to estimate activ-  
63 ity patterns at arbitrary locations in each person’s brain (i.e., independent of their electrode  
64 placements). We test our SuperEEG approach using two large datasets of intracranial record-  
65 ings [7, 8, 12, 16–19, 21, 23, 30–32, 35, 40]. We show that the SuperEEG algorithm recovers  
66 signals well from electrodes that were held out of the training dataset. We also examine the  
67 factors that influence how accurately activity may be estimated (recovered), which may have  
68 implications for electrode design and placement in neurosurgical applications.

## 69 Approach

70 The SuperEEG approach to inferring high temporal resolution full-brain activity patterns is  
71 outlined and summarized in Figure 1. We describe (in this section) and evaluate (in *Results*) our  
72 approach using a two large previously collected dataset comprising multi-session intracranial  
73 recordings. Dataset 1 comprises multi-session recordings taken from 6876 electrodes implanted

74 in the brains of 88 epilepsy patients [21, 23, 30–32]. Each recording session lasted from 0.2–  
75 3 h (total recording time: 0.3–14.2 h; Fig. S4A). During each recording session, the patients  
76 participated in a free recall list learning task, which lasted for up to approximately 1 h. In  
77 addition, the recordings included “buffer” time (the length varied by patient) before and after  
78 each experimental session, during which the patients went about their regular hospital activities  
79 (confined to their hospital room, and primarily in bed). These additional activities included  
80 interactions with medical staff and family, watching television, reading, and other similar  
81 activities. For the purposes of the Dataset 1 analyses presented here, we aggregated all data  
82 across each recording session, including recordings taken during the main experimental task  
83 as well as during non-experimental time. We used Dataset 1 to develop our main SuperEEG  
84 approach, and to examine the extent to which SuperEEG might be able to generate task-general  
85 predictions. Dataset 2 comprised multi-session recordings from 4436 electrodes implanted in  
86 the brains of 40 epilepsy patients [7, 8, 12, 16–19, 35, 40]. Each recording session lasted from  
87 0.4–2.2 h (total recording time: 0.4–6.6 h; Fig. S4B). Whereas Dataset 1 included recordings  
88 taken as the patients participated in a variety of activities, Dataset 2 included recordings taken  
89 as each patient performed each of two specific experimental memory tasks: a random word list  
90 free recall task (Experiment 1) and a categorized word list free recall task (Experiment 2). We  
91 used Dataset 2 to further examine the ability of SuperEEG to generalize its predictions within  
92 versus across tasks. Figure S4 provides additional information about both datasets.

93 We first applied fourth order Butterworth notch filter to remove 60 Hz ( $\pm .5$  Hz) line noise  
94 from every recording (from every electrode). Next, we downsampled the recordings (regardless  
95 of the original samplerate) to 250 Hz. (This downsampling step served to both normalize for  
96 differences in sampling rates across patients and to ease the computational burden of our sub-  
97 sequent analyses.) We then excluded any electrodes that showed putative epileptiform activity.  
98 Specifically, we excluded from further analysis any electrode that exhibited an average kurtosis

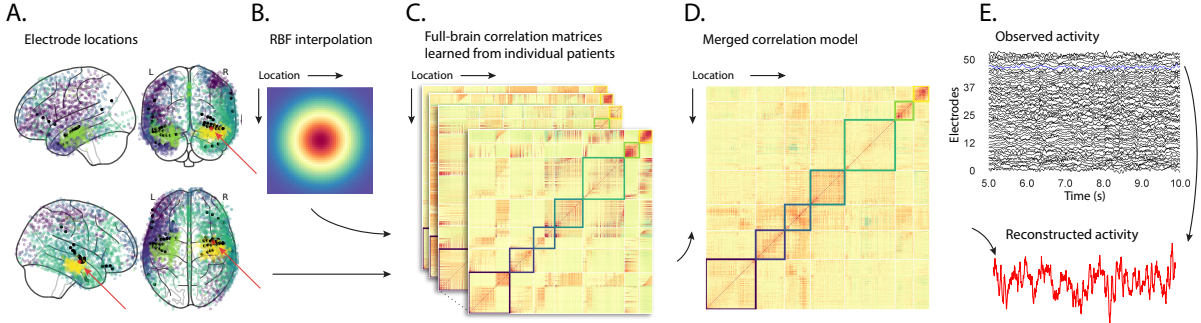


**Figure 1: Methods overview.** **A. Electrode locations.** Each dot reflects the location of a single electrode implanted in the brain of a Dataset 1 patient. A held-out recording location from one patient is indicated in red, and the patient’s remaining electrodes are indicated in black. The electrodes from the remaining patients are colored by  $k$ -means cluster (computed using the full-brain correlation model shown in Panel D). **B. Radial basis function kernel.** Each electrode contributed by the patient (black) weights on the full set of locations under consideration (all dots in Panel A, defined as  $\bar{R}$  in the text). The weights fall off with positional distance (in MNI space) according to an RBF. **C. Per-patient correlation matrices.** After computing the pairwise correlations between the recordings from each patient’s electrodes, we use RBF-weighted averages to estimate correlations between all locations in  $\bar{R}$ . We obtain an estimated full-brain correlation matrix using each patient’s data. **D. Merged correlation model.** We combine the per-patient correlation matrices (Panel C) to obtain a single full-brain correlation model that captures information contributed by every patient. Here we have sorted the rows and columns to reflect  $k$ -means clustering labels [using  $k=7$ ; 41], whereby we grouped locations based on their correlations with the rest of the brain (i.e., rows of the matrix displayed in the panel). The boundaries denote the cluster groups. The rows and columns of Panel C have been sorted using the Panel D-derived cluster labels. **E. Reconstructing activity throughout the brain.** Given the observed recordings from the given patient (shown in black; held-out recording is shown in blue), along with a full-brain correlation model (Panel D), we use Equation 12 to reconstruct the most probable activity at the held-out location (red).

99 of 10 or greater across all of that patient’s recording sessions. We also excluded any patients  
100 with fewer than 2 electrodes that passed this criteria, as the SuperEEG algorithm requires  
101 measuring correlations between 2 or more electrodes from each patient. For Dataset 1, this  
102 yielded clean recordings from 4168 electrodes implanted throughout the brains of 67 patients  
103 (Fig. 1A); for Dataset 2, this yielded clean recordings from 3159 electrodes from 24 patients.  
104 Each individual patient contributes electrodes from a limited set of brain locations, which we  
105 localized in a common space [MNI152; 10]; an example Dataset 1 patient’s 54 electrodes that  
106 passed the predefined kurtosis test are highlighted in black and red.

The recording from a given electrode is maximally informative about the activity of the neural tissue immediately surrounding its recording surface. However, brain regions that are distant from the recording surface of the electrode also contribute to the recording, albeit (*ceteris paribus*) to a much lesser extent. One mechanism underlying these contributions is volume conduction. The precise rate of falloff due to volume conduction (i.e., how much a small volume of brain tissue at location  $x$  contributes to the recording from an electrode at location  $\eta$ ) depends on the size of the recording surface, the electrode’s impedance, and the conductance profile of the volume of brain between  $x$  and  $\eta$ . As an approximation of this intuition, we place a Gaussian radial basis function (RBF) at the location  $\eta$  of each electrode’s recording surface (Fig. 1B). We use the values of the RBF at any brain location  $x$  as a rough estimate of how much structures around  $x$  contributed to the recording from location  $\eta$ :

$$\text{rbf}(x|\eta, \lambda) = \exp \left\{ -\frac{\|x - \eta\|^2}{\lambda} \right\}, \quad (1)$$

107 where the width variable  $\lambda$  is a parameter of the algorithm (which may in principle be set  
108 according to location-specific tissue conductance profiles) that governs the level of spatial  
109 smoothing. In choosing  $\lambda$  for the analyses presented here, we sought to maximize spatial  
110 resolution (which implies a small value of  $\lambda$ ) while also maximizing the algorithm’s ability  
111 to generalize to any location throughout the brain, including those without dense electrode

coverage (which implies a large value of  $\lambda$ ). Here we set  $\lambda = 20$ , guided in part by our prior work [22, 24], and in part by examining the brain coverage with non-zero weights achieved by placing RBFs at each electrode location in Dataset 1 and taking the sum (across all electrodes) at each voxel in a  $4 \text{ mm}^3$  MNI brain. (We then held  $\lambda$  fixed for our analyses of Dataset 2.) We note that this value could in theory be further optimized, e.g., using cross validation or a formal model [e.g., 24].

A second mechanism whereby a given region  $x$  can contribute to the recording at  $\eta$  is through (direct or indirect) anatomical connections between structures near  $x$  and  $\eta$ . We use temporal correlations in the data to estimate these anatomical connections [2]. Let  $\bar{R}$  be the set of locations at which we wish to estimate local field potentials, and let  $R_s \subseteq \bar{R}$  be set of locations at which we observe local field potentials from patient  $s$  (excluding the electrodes that did not pass the kurtosis test described above). In the analyses below we define  $\bar{R} = \cup_{s=1}^S R_s$ . We can calculate the expected inter-electrode correlation matrix for patient  $s$ , where  $C_{s,k}(i, j)$  is the correlation between the time series of voltages for electrodes  $i$  and  $j$  from subject  $s$  during session  $k$ , using:

$$\bar{C}_s = r\left(\frac{1}{n}\left(\sum_{k=1}^n z(C_{s,k})\right)\right), \text{ where} \quad (2)$$

$$z(r) = \frac{\log(1+r) - \log(1-r)}{2} \text{ is the Fisher } z\text{-transformation and} \quad (3)$$

$$z^{-1}(z) = r(z) = \frac{\exp(2z) - 1}{\exp(2z) + 1} \text{ is its inverse.} \quad (4)$$

Next, we use Equation 1 to construct a number of to-be-estimated locations by number of patient electrode locations weight matrix,  $W_s$ . Specifically,  $W_s$  approximates how informative the recordings at each location in  $R_s$  are in reconstructing activity at each location in  $\bar{R}$ , where the contributions fall off with an RBF according to the distances between the corresponding locations:

$$W_s(i, j) = \text{rbf}(i|j, \lambda). \quad (5)$$

Given this weight matrix,  $W_s$ , and the observed inter-electrode correlation matrix for patient  $s$ ,  $\bar{C}_s$ , we can estimate the correlation matrix for all locations in  $\bar{R}$  ( $\hat{C}_s$ ; Fig. 1C) using:

$$\hat{N}_s(x, y) = \sum_{i=1}^{|R_s|} \sum_{j=1}^{i-1} W(x, i) \cdot W(y, j) \cdot z(\bar{C}_s(i, j)) \quad (6)$$

$$\hat{D}_s(x, y) = \sum_{i=1}^{|R_s|} \sum_{j=1}^{i-1} W(x, i) \cdot W(y, j). \quad (7)$$

$$\hat{C}_s = r\left(\frac{\hat{N}_s}{\hat{D}_s}\right). \quad (8)$$

After estimating the numerator ( $\hat{N}_s$ ) and denominator ( $\hat{D}_s$ ) placeholders for each  $\hat{C}_s$ , we aggregate these estimates across the  $S$  patients to obtain a single expected full-brain correlation matrix ( $\hat{K}$ ; Fig. 1D):

$$\hat{K} = r\left(\frac{\sum_{s=1}^S \hat{N}_s}{\sum_{s=1}^S \hat{D}_s}\right). \quad (9)$$

Intuitively, the numerators capture the general structures of the patient-specific estimates of full-brain correlations, and the denominators account for which locations were near the implanted electrodes in each patient. To obtain  $\hat{K}$ , we compute a weighted average across the estimated patient-specific full-brain correlation matrices, where patients with observed electrodes near a particular set of locations in  $\hat{K}$  contribute more to the estimate.

Having used the multi-patient data to estimate a full-brain correlation matrix at the set of locations in  $\bar{R}$  that we wish to know about, we next use  $\hat{K}$  to estimate activity patterns everywhere in  $\bar{R}$ , given observations at only a subset of locations in  $\bar{R}$  (Fig. 1E).

Let  $\alpha_s$  be the set of indices of patient  $s$ 's electrode locations in  $\bar{R}$  (i.e., the locations in  $R_s$ ), and let  $\beta_s$  be the set of indices of all other locations in  $\bar{R}$ . In other words,  $\beta_s$  reflects the locations

<sup>144</sup> in  $\bar{R}$  where we did not observe a recording for patient  $s$  (these are the recording locations we  
<sup>145</sup> will want to fill in using SuperEEG). We can sub-divide  $\hat{K}$  as follows:

$$\hat{K}_{\beta_s, \alpha_s} = \hat{K}(\beta_s, \alpha_s), \text{ and} \quad (10)$$

$$\hat{K}_{\alpha_s, \alpha_s} = \hat{K}(\alpha_s, \alpha_s). \quad (11)$$

<sup>146</sup> Here  $\hat{K}_{\beta_s, \alpha_s}$  represents the correlations between the “unknown” activity at the locations in  $\beta_s$   
<sup>147</sup> and the observed activity at the locations in  $\alpha_s$ , and  $\hat{K}_{\alpha_s, \alpha_s}$  represents the correlations between  
<sup>148</sup> the observed recordings (at the locations in  $\alpha_s$ ).

<sup>149</sup> Let  $Y_{s,k,\alpha_s}$  be the number-of-timepoints ( $T$ ) by  $|\alpha_s|$  matrix of (observed) voltages from the  
<sup>150</sup> electrodes in  $\alpha_s$  during session  $k$  from patient  $s$ . Then we can estimate the voltage from patient  
<sup>151</sup>  $s$ ’s  $k^{th}$  session at the locations in  $\beta_s$  using [27]:

$$\hat{Y}_{s,k,\beta_s} = ((\hat{K}_{\beta_s, \alpha_s} \cdot \hat{K}_{\alpha_s, \alpha_s}^{-1}) \cdot Y_{s,k,\alpha_s}^T)^T. \quad (12)$$

<sup>152</sup> This equation is the foundation of the SuperEEG algorithm. Whereas we observe recordings  
<sup>153</sup> only at the locations indexed by  $\alpha_s$ , Equation 12 allows us to estimate the recordings at all loca-  
<sup>154</sup> tions indexed by  $\beta_s$ , which we can define *a priori* to include any locations we wish, throughout  
<sup>155</sup> the brain. This yields estimates of the time-varying voltages at *every* location in  $\bar{R}$ , provided that  
<sup>156</sup> we define  $\bar{R}$  in advance to include the union of all of the locations in  $R_s$  and all of the locations  
<sup>157</sup> at which we wish to estimate recordings (i.e., a timeseries of voltages).

<sup>158</sup> We designed our approach to be agnostic to electrode impedances, as electrodes that do not  
<sup>159</sup> exist do not have impedances. Therefore our algorithm recovers voltages in standard deviation  
<sup>160</sup> ( $z$ -scored) units rather than attempting to recover absolute voltages. (This property reflects  
<sup>161</sup> the fact that  $\hat{K}_{\beta_s, \alpha_s}$  and  $\hat{K}_{\alpha_s, \alpha_s}$  are correlation matrices rather than covariance matrices.) Also,  
<sup>162</sup> note that Equation 12 requires computing a  $T$  by  $T$  matrix, which can become computationally

163 intractable when  $T$  is very large (e.g., for the patient highlighted in Fig. 2,  $T = 12786750$ ).  
164 However, because Equation 12 is time invariant, we may compute  $Y_{s,k,\beta_s}$  in a piecewise manner  
165 by filling in  $Y_{s,k,\beta_s}$  one row at a time (using the corresponding samples from  $Y_{s,k,\alpha_s}$ ).

166 The SuperEEG algorithm described above and in Figure 1 allows us to estimate, up to a  
167 constant scaling factor, local field potentials (LFPs) for each patient at all arbitrarily chosen  
168 locations in the set  $\bar{R}$ , even if we did not record that patient's brain at all of those locations. We next  
169 turn to an evaluation of the accuracy of those estimates.

## 170 Results

171 We used a cross-validation approach to test the accuracy with which the SuperEEG algorithm  
172 reconstructs activity throughout the brain. For each patient in turn, we estimated full-brain  
173 correlation matrices (Eqn. 9) using data from all of the *other* patients. This step ensured that the  
174 data we were reconstructing could not also be used to estimate the between-location correlations  
175 that drove the reconstructions via Equation 12 (otherwise the analysis would be circular). For  
176 that held-out patient, for each of their electrodes in turn, we used Equation 12 to reconstruct  
177 activity at the held-out electrode location, using the correlation matrix learned from all other  
178 patients' data as  $\hat{K}$ , and using activity recorded from the other electrodes from the held-out  
179 patient as  $Y_{s,k,\alpha_s}$ . We then asked: how closely did each of the SuperEEG-estimated recordings  
180 at those electrodes match the observed recordings from those electrodes (i.e., how closely did  
181 the estimated  $\hat{Y}_{s,k,\beta_s}$  match the observed  $Y_{s,k,\beta_s}$ ?).

182 To illustrate our approach, we first examine an individual held-out raw LFP trace and its  
183 associated SuperEEG-derived reconstruction. Figure 2A displays the observed LFP from the red  
184 electrode in Figure 1A (blue), and its associated reconstruction (red), during a 5 s time window  
185 during one of the example patient's six recording sessions. The two traces match closely  
186 ( $r = 0.86, p < 10^{-10}$ ). Figure 2B displays a two-dimensional histogram of the actual versus

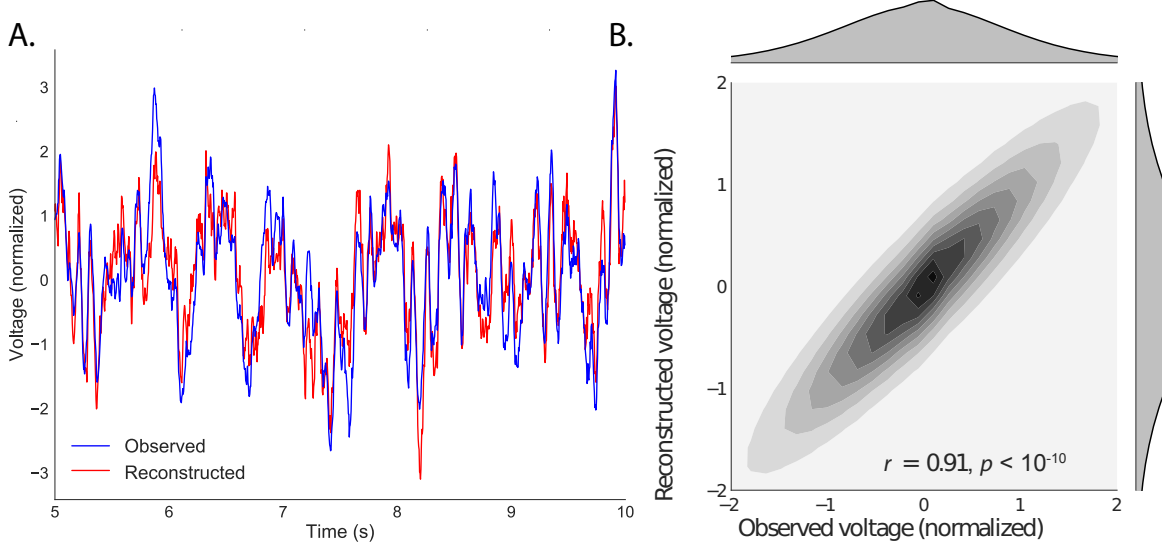


**Figure 2: Observed and reconstructed LFP from a single electrode.** **A. Example LFP.** A 5 s recording from the red electrode in Figure 1A is displayed in blue, and the reconstructed LFP during the same time window is shown in red. **B. Observed versus reconstructed LFP over 14.2 hours.** The two-dimensional histogram reflects the relation between distributions of observed versus reconstructed voltages from one patient, across the 14.2 hours of recorded data collected over 6 recording sessions. The correlation reported in the panel is between the observed and reconstructed voltages. Both panels: all voltages are represented in standard deviation units (computed within session).

reconstructed voltages for the entire 14.2 total hours of recordings from the example electrode (correlation:  $r = 0.91, p < 10^{-10}$ ). This example confirms that the SuperEEG algorithm recovers the recordings from this single electrode well. Next, we used this general approach to quantify the algorithm's performance across the full dataset.

For each held-out electrode, from each held-out patient in turn, we computed the average correlation (across recording sessions) between the SuperEEG-reconstructed voltage traces and the observed voltage traces from that electrode. For this analysis we set  $\bar{R}$  to be the union of all electrode locations across all patients. This yielded a single correlation coefficient for each electrode location in  $\bar{R}$ , reflecting how well the SuperEEG algorithm was able to recover the recording at that location by incorporating data across patients (black histogram in Fig. 3A, map

197 in Fig. 3C). The observed distribution of correlations was centered well above zero (mean: 0.52;  
198  $t$ -test comparing mean of distribution of  $z$ -transformed average patient correlation coefficients  
199 to 0:  $t(66) = 25.08, p < 10^{-10}$ ), indicating that the SuperEEG algorithm recovers held-out  
200 activity patterns substantially better than random guessing.

201 As a stricter benchmark, we compared the quality of these across-participant reconstructions  
202 (i.e., computed using a correlation model learned from other patients' data) to reconstructions  
203 generated using a correlation model trained using the in-patient's data. In other words, for  
204 this within-patient benchmark analysis we estimated  $\hat{C}_s$  (Eqn. 8) for each patient in turn, using  
205 recordings from all of that patient's electrodes except at the location we were reconstructing.  
206 These within-patient reconstructions serve as an estimate of how well data from all of the  
207 other electrodes from that single patient may be used to estimate held-out data from the  
208 same patient. This allows us to ask how much information about the activity at a given  
209 electrode might be inferred through (a) volume conductance or other sources of "leakage"  
210 from activity patterns measured from the patient's other electrodes and (b) across-electrode  
211 correlations learned from that single patient. As shown in Figure 3A (gray histogram), the  
212 distribution of within-patient correlations was centered well above zero (mean: 0.32;  $t$ -test  
213 comparing mean of distribution of  $z$ -transformed average patient correlation coefficients to 0:  
214  $t(66) = 15.16, p < 10^{-10}$ ). However, the across-patient correlations were substantially higher  
215 ( $t$ -test comparing average  $z$ -transformed within versus across patient electrode correlations:  
216  $t(66) = 9.62, p < 10^{-10}$ ). This is an especially conservative test, given that the across-patient  
217 SuperEEG reconstructions exclude (from the correlation matrix estimates) all data from the  
218 patient whose data is being reconstructed. We repeated each of these analyses on a second  
219 independent dataset and found similar results (Fig. 3B, D; within versus across reconstruction  
220 accuracy:  $t(23) = 6.93, p < 10^{-5}$ ). We also replicated this result separately for each of the two  
221 experiments from Dataset 2 (Fig. S1). This overall finding, that reconstructions of held-out

222 data using correlation models learned from *other* patient's data yield higher reconstruction  
223 accuracy than correlation models learned from the patient whose data is being reconstructed,  
224 has two important implications. First, it implies that distant electrodes provide additional  
225 predictive power to the data reconstructions beyond the information contained solely in nearby  
226 electrodes. (This follows from the fact that each patient's electrodes are implanted in a unique  
227 set of locations, so for any given electrode the closest electrodes in the full dataset are likely to  
228 come from the same patient.) Second, it implies that the spatial correlations learned using the  
229 SuperEEG algorithm are, to some extent, similar across people.

230 The recordings we analyzed from Dataset 1 comprised data collected as the patients per-  
231 formed a variety of (largely idiosyncratic) tasks throughout each day's recording session. That  
232 we observed reliable reconstruction accuracy across patients suggests that the spatial correla-  
233 tions derived from the SuperEEG algorithm are, to some extent, similar across tasks. We tested  
234 this finding more explicitly using Dataset 2. In Dataset 2, the recordings were limited to times  
235 when each patient was participating in each of two experiments (Experiment 1, a random-word  
236 list free recall task, and Experiment 2, a categorized list free recall task). We wondered whether  
237 a correlation model learned from data from one experiment might yield good predictions of  
238 data from the other experiment. Further, we wondered about the extent to which it might be  
239 beneficial or harmful to combine data across tasks.

240 To test the task-specificity of the SuperEEG-derived correlation models, we repeated the  
241 above within- and across-patient cross validation procedures separately for Experiment 1 and  
242 Experiment 2 data from Dataset 2. We then compared the reconstruction accuracies for held-out  
243 electrodes, for models trained within versus across the two experiments, or combining across  
244 both experiments (Fig. S2). In every case we found that across-patient models trained using  
245 data from all other patients out-performed within-patient models trained on data only from the  
246 subject contributing the given electrode ( $ts(24) > 6.50, ps < 10^{-5}$ ). All reconstruction accuracies

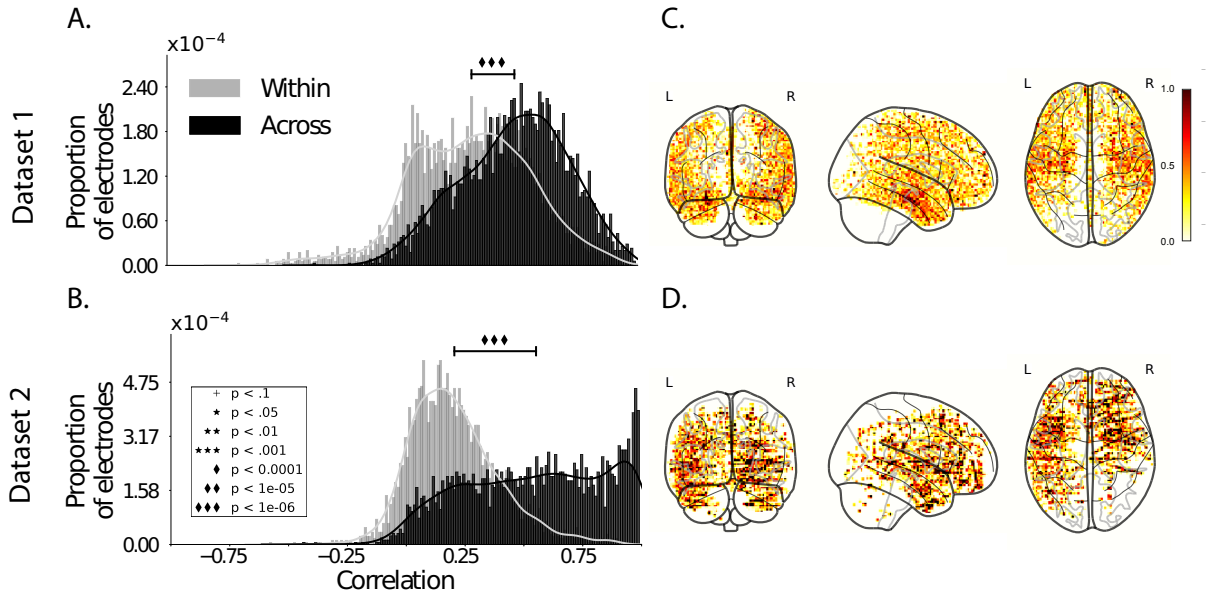


**Figure 3: Reconstruction quality across all electrodes in two ECoG datasets. A. Distributions of correlations between observed versus reconstructed activity by electrode, for Dataset 1.** The across-patient distribution (black) reflects reconstruction accuracy (correlation) using a correlation model learned from all but one patient's data, and then applied to that held-out patient's data. The within-patient distribution (gray) reflects performance using a correlation model learned from the same patient who contributed the to-be-reconstructed electrode. **B. Distributions of correlations for Dataset 2.** This panel is in the same format as Panel A, but reflects results obtained from Dataset 2. The histograms aggregate data across both Dataset 2 experiments; for results broken down by experiment see Figure S3. **C.-D. Reconstruction performance by location.** Each dot reflects the location of a single implanted electrode from Dataset 1 (Panel C) or Dataset 2 (Panel D). The dot colors denote the average across-session correlation, using the across-patient correlation model, between the observed and reconstructed activity at the given electrode location.

247 also reliably exceeded chance performance ( $t_{s(24)} > 8.00, p < 10^{-8}$ ). Average reconstruction  
248 accuracy was highest for the across-patient models limited to data from the same experiment  
249 (mean accuracy: 0.68); next-highest for the across-patient models that combined data across  
250 both experiments (mean accuracy: 0.61); and lowest for models trained across task (mean  
251 accuracy: 0.47). This result also held for each of the Dataset 2 experiments individually  
252 (Fig. S3). Taken together, these results indicate that there are reliable commonalities in the spatial  
253 correlations of full-brain activity across tasks, but that there are also reliable differences in these  
254 spatial correlations across tasks. Whereas reconstruction accuracy benefits from incorporating  
255 data from other patients, reconstruction accuracy is highest when constrained to within-task  
256 data, or data that includes a variety of tasks (e.g., Dataset 1, or combining across the two Dataset  
257 2 experiments).

258 Although both datasets we examined provide good full-brain coverage (when considering  
259 data from every patient; e.g. Fig. 3C, D), electrodes are not placed uniformly throughout the  
260 brain. For example, electrodes are more likely to be implanted in regions like the medial  
261 temporal lobe (MTL), and are rarely implanted in occipital cortex (Fig. 4A, B). Separately for  
262 each dataset, for each voxel in the  $4 \text{ mm}^3$  voxel MNI152 brain, we computed the proportion  
263 of electrodes in the dataset that were contained within a 20 MNI unit radius sphere centered  
264 on that voxel. We defined the *density* at that location as this proportion. Across Datasets  
265 1 and 2, the electrode placement densities were similar (correlation by voxel:  $r = 0.56, p <$   
266  $10^{-10}$ ). We wondered whether regions with good coverrage might be associated with better  
267 reconstruction accuracy (e.g. Fig. 3C, D indicate that many electrodes in the MTL have relatively  
268 high reconstruction accuracy, and occipital electrodes tend to have relatively low reconstruction  
269 accuracy). To test whether this held more generally across the entire brain, for each dataset  
270 we computed the electrode placement density for each electrode from each patient (using  
271 the proportion of *other* patients' electrodes within 20 MNI units of the given electrode). We

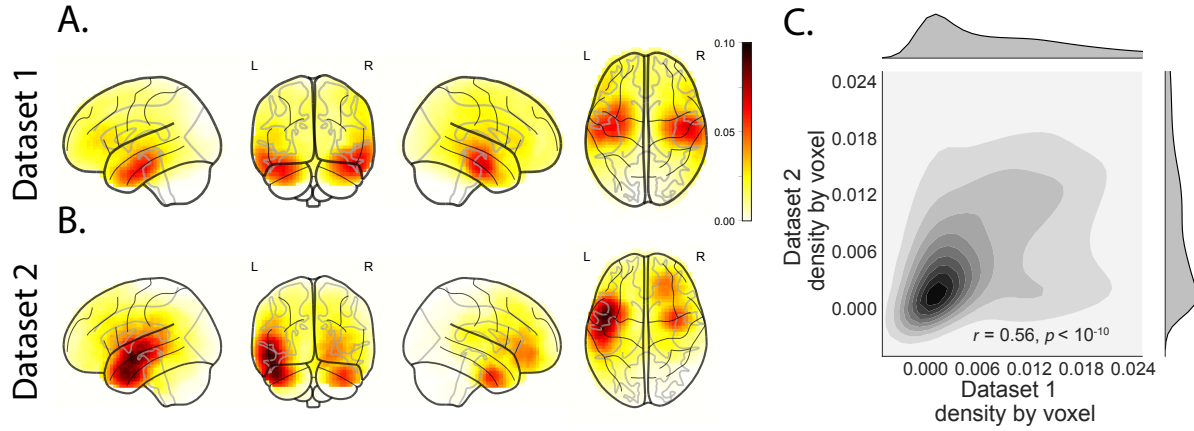


**Figure 4: Electrode sampling density by location.** **A. Electrode sampling density by voxel in Dataset 1.** Each voxel is colored by the proportion of total electrodes in the dataset that are located within a 20 MNI unit radius sphere centered on the given voxel. **B. Electrode sampling density by voxel in Dataset 2.** This panel displays the sampling density map for Dataset 2, in the same format as Panel A. **C. Correspondence in sampling density by voxel across Datasets 1 and 2.** The two-dimensional histogram displays the by-voxel densities in the two Datasets, and the one-dimensional histograms display the proportions of voxels in each dataset with the given density value. The correlation reported in the panel is across voxels in the  $4 \text{ mm}^3$  MNI brain.

272 then correlated these density values with the across-patient reconstruction accuracies for each  
 273 electrode. Contrary to our expectation, rather than positive correlations, we found weak (but  
 274 reliable) negative correlations between reconstruction accuracy and density for both datasets  
 275 (Dataset 1:  $r = -0.07, p < 10^{-5}$ ; Dataset 2:  $r = -0.18, p < 10^{-10}$ ). This indicates that the  
 276 reconstruction accuracies we observed are not driven solely by sampling density, but rather  
 277 may also reflect higher order properties of neural dynamics such as functional correlations  
 278 between distant voxels [3].

279 In neurosurgical applications where one wishes to infer full-brain activity patterns, can our  
 280 framework yield insights into where the electrodes should be placed? A basic assumption of our  
 281 approach (and of most prior ECoG work) is that electrode recordings are most informative about  
 282 the neural activity near the recording surface of the electrode. But if we consider that activity  
 283 patterns throughout the brain are meaningfully correlated, are there particular implantation

locations that, if present in a patient’s brain, yield especially high reconstruction accuracies throughout the rest of the brain? For example, one might hypothesize that brain structures that are heavily interconnected with many other structures could be more informative about full-brain activity patterns than comparatively isolated structures.

To gain insights into whether particular electrode locations might be especially informative, we first computed the average reconstruction accuracy across all of each patient’s electrodes (using the across-patients cross validation test; black histograms in Fig. 3A and B). We labeled each patient’s electrodes in each dataset with the average reconstruction accuracy for that patient. In other words, we assigned every electrode from each given patient the same value, reflecting how well the activity patterns at those electrodes were reconstructed on average. Next, for each voxel in the 4 mm<sup>3</sup> MNI brain, we computed the average value across any electrode (from any patient) that came within 20 MNI units of that voxel’s center. Effectively, we computed an *information score* for each voxel, reflecting the average reconstruction accuracy across any patients with electrodes near each voxel—where the averages were weighted to reflect patients who had more electrodes implanted near that location. This yielded a single map for each dataset, highlighting regions that are potentially promising implantation targets in terms of providing full-brain activity information via SuperEEG (Fig. 5A, B). Despite task and patient differences across the two datasets, we nonetheless found that the maps of the most promising implantation targets derived from both datasets were similar (voxelwise correlation between information scores across the two datasets:  $r = 0.03, p < 10^{-10}$ ). While the correspondence between the two maps was not perfect, our finding that there were some commonalities between the two maps lends support to the notion that different brain areas are differently informative about full-brain activity patterns. Further, we found the intersection of the top 10% of the most informative voxels between the two datasets (Fig. S5) and found gray matter regions like the right postcentral gyrus, right supramarginal gyrus, and the right nucleus accumbens that

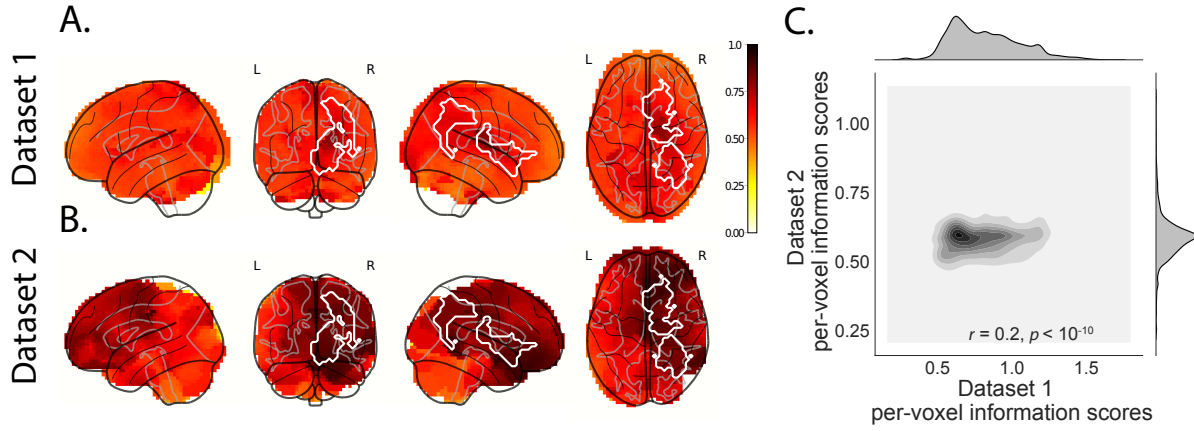


**Figure 5: Most informative electrode locations.** **A. Dataset 1 information score by voxel.** The voxel colors reflect the weighted average reconstruction accuracy across all electrodes from any patients with at least one electrode within 20 MNI units of the given voxel. **B. Dataset 2 information score by voxel.** This panel is in the same format as Panel A. In both panels the contours indicate the intersections between the top 10% most informative voxels in each map. **C. Correspondence in information scores by voxel across Datasets 1 and 2.** Same format as Figure 4C.

exhibited strong information scores in both datasets may be especially promising implantation targets.

## Discussion

Are our brain's networks static or dynamic? And to what extent are the network properties of our brains stable across people and tasks? One body of work suggests that our brain's *functional* networks are dynamic [e.g., 24], person-specific [e.g., 9], and task-specific [e.g., 39]. In contrast, although the gross anatomical structure of our brains changes meaningfully over the course of years as our brains develop, on the timescales of typical neuroimaging experiments (i.e., hours to days) our anatomical networks are largely stable [e.g., 4]. Further, many aspects of brain anatomy, including white matter structure, are largely preserved across people [e.g., 15, 26, 37]. There are several possible means of reconciling this apparent inconsistency between dynamic person- and task-specific functional networks versus stable anatomical

321 networks. For example, relatively small magnitude anatomical differences across people may  
322 be reflected in reliable functional connectivity differences. Along these lines, one recent study  
323 found that diffusion tensor imaging (DTI) structural data is similar across people, but may be  
324 used to predict person-specific resting state functional connectivity data [2]. Similarly, other  
325 work indicates that task-specific functional connectivity may be predicted by resting state func-  
326 tional connectivity data [5, 38]. Another (potentially complementary) possibility is that our  
327 functional networks are constrained by anatomy, but nevertheless exhibit (potentially rapid)  
328 task-dependent changes [e.g., 36].

329 Here we have taken a model-based approach to studying whether high spatiotemporal  
330 resolution activity patterns throughout the human brain may be explained by a static connec-  
331 tive model that is shared across people and tasks. Specifically, we trained a model to take  
332 in recordings from a subset of brain locations, and then predicted activity patterns during the  
333 same interval, but at *other* locations that were held out from the model. Our model, based on  
334 Gaussian process regression, was built on three general hypotheses about the nature of the  
335 correlational structure of neural activity (each of which we tested). First, we hypothesized that  
336 functional correlations are stable over time and across tasks. We found that, although aspects  
337 of the patients' functional correlations that were stable across tasks, we achieved better recon-  
338 struction accuracy when we trained the model on within-task data [we acknowledge that our  
339 general approach could potentially be extended to better model across-task changes, following  
340 5, 38, and others]. Second, we hypothesized that some of the correlational structure of peo-  
341 ple's brain activity is similar across individuals. Consistent with this hypothesis, our model  
342 explained the data best when we trained the correlation model using data from *other* patients—  
343 even when compared to a correlation model trained on the same patient's data. Third, we  
344 resolved ambiguities in the data by hypothesizing that neural activity from nearby sources will  
345 tend to be similar, all else being equal. This hypothesis was supported through our finding that

346 all of the models we trained that incorporated this spatial smoothness assumption predicted  
347 held-out data well above chance.

348 One potential limitation of our approach is that it does not provide a natural means of  
349 estimating the precise timing of single-neuron action potentials. Prior work has shown that  
350 gamma band and broadband activity in the LFP may be used to estimate the firing rates of  
351 neurons that underly the population contributing to the LFP [6, 14, 20, 25]. Because SuperEEG  
352 reconstructs LFPs throughout the brain, one could in principle use gamma or broadband power  
353 in the reconstructed signals to estimate the corresponding firing rates (though not the timings  
354 of individual action potentials).

355 Beyond providing a means of estimating ongoing activity throughout the brain using al-  
356 ready implanted electrodes, our work also has implications for where to place the electrodes in  
357 the first place. Electrodes are typically implanted to maximize coverage of suspected epilep-  
358 togenic tissue. However, our findings suggest that this approach could be further optimized.  
359 Specifically, one could leverage not only the non-invasive recordings taken during an initial  
360 monitoring period (as is currently done routinely), but also recordings collected from other  
361 patients. We could then ask: given what we learn from other patients' data (and potentially  
362 from the scalp EEG recordings of this new patient), where should we place a fixed number of  
363 electrodes to maximize our ability to map seizure foci? As shown in Figure 5, recordings from  
364 different locations are differently informative in terms of reconstructing the spatiotemporal  
365 activity patterns throughout the brain. This property might be leveraged in decisions about  
366 where to surgically implant electrodes in future patients.

## 367 **Concluding remarks**

368 Over the past several decades, neuroscientists have begun to leverage the strikingly profound  
369 mathematical structure underlying the brain's complexity to infer how our brains carry out

370 computations to support our thoughts, actions, and physiological processes. Whereas tradi-  
371 tional beamforming techniques rely on geometric source-localization of signals measured at the  
372 scalp, here we propose an alternative approach that leverages the rich correlational structure  
373 of two large datasets of human intracranial recordings. In doing so, we are one step closer to  
374 observing, and perhaps someday understanding, the full spatiotemporal structure of human  
375 neural activity.

## 376 **Code availability**

377 We have published an open-source toolbox implementing the SuperEEG algorithm. It may  
378 be downloaded [here](#). Additionally, we have provided notebooks for all analyses and figures  
379 reported here.

## 380 **Data availability**

381 The dataset analyzed in this study was generously shared by Michael Kahana. A portion of  
382 Dataset 1 may be downloaded [here](#). Dataset 2 may be downloaded [here](#).

## 383 **Acknowledgements**

384 We are grateful for useful discussions with Luke J. Chang, Uri Hasson, Josh Jacobs, Michael  
385 Kahana, and Matthijs van der Meer. We are also grateful to Michael Kahana for generously  
386 sharing the ECoG data we analyzed in our paper, which was collected under NIMH grant  
387 MH55687 and DARPA RAM Cooperative Agreement N66001-14-2-4-032, both to MJK. Our  
388 work was also supported in part by NSF EPSCoR Award Number 1632738 and by a sub-  
389 award of DARPA RAM Cooperative Agreement N66001-14-2-4-032 to JRM. The content is solely  
390 the responsibility of the authors and does not necessarily represent the official views of our  
391 supporting organizations.

392 **Author Contributions**

393 J.R.M conceived and initiated the project. L.L.W.O. and A.C.H. performed the analyses. J.R.M.  
394 and L.L.W.O. wrote the manuscript.

395 **Author Information**

396 Reprints and permissions information is available at [www.nature.com/reprints](http://www.nature.com/reprints). The authors  
397 declare no competing financial interests. Readers are welcome to comment on the online  
398 version of the paper. Publisher's note: Springer Nature remains neutral with regard to jurisdic-  
399 tional claims in published maps and institutional affiliations. Correspondence and requests for  
400 materials should be addressed to J.R.M. ([jeremy.r.manning@dartmouth.edu](mailto:jeremy.r.manning@dartmouth.edu)).

401 **References**

- 402 [1] Baillet, S., Mosher, J. C., and Leahy, R. M. (2001). Electromagnetic brain mapping. *IEEE  
403 Signal Processing Magazine*, 18:14–30.
- 404 [2] Becker, C. O., Pequito, S., Pappas, G. J., Miller, M. B., adn D S Bassett, S. T. G., and Preciado,  
405 V. M. (2018). Spectral mapping of brain functional connectivity from diffusion imaging.  
406 *Scientific Reports*, 8(1411):<https://doi.org/10.1038/s41598-017-18769-x>.
- 407 [3] Betzel, R. F., Medaglia, J. D., Kahn, A. E., Soffer, J., Schonhaut, D. R., and Bassett, D. S.  
408 (2017). Inter-regional ecog correlations predicted by communication dynamics, geometry,  
409 and correlated gene expression. *arXiv*, page 1706.06088.
- 410 [4] Casey, B. J., Giedd, J. N., and Thomas, K. M. (2000). Structural and functional brain devel-  
411 opment and its relation to cognitive development. *Biological Psychology*, 54(1–3):241–257.
- 412 [5] Cole, M. W., Ito, T., Bassett, D. S., and Schultz, D. H. (2016). Activity flow over resting-state  
413 networks shapes cognitive task activations. *Nature Neuroscience*, 19(12):1718–1726.

- 414 [6] Crone, N. E., Korzeniewska, A., and Franaszczuk, P. (2011). Cortical gamma responses:  
415 searching high and low. *International Journal of Psychophysiology*, 79(1):9–15.
- 416 [7] Ezzyat, Y., Kragel, J. E., Burke, J. F., Levy, D. F., Lyalenko, A., Wanda, P., O’Sullivan, L.,  
417 Hurley, K. B., Busygin, S., Pedisich, I., Sperling, M. R., Worrell, G. A., Kucewicz, M. T., Davis,  
418 K. A., Lucas, T. H., Inman, C. S., Lega, B. C., Jobst, B. C., Sheth, S. A., Zaghloul, K., Jutras,  
419 M. J., Stein, J. M., Das, S. R., Gorniak, R., Rizzuto, D. S., and Kahana, M. J. (2017). Direct  
420 brain stimulation modulates encoding states and memory performance in humans. *Current  
Biology*, 27:1–8.
- 422 [8] Ezzyat, Y., Wanda, P. A., Levy, D. F., Kadel, A., Aka, A., Pedisich, I., Sperling, M. R.,  
423 Sharan, A. D., Lega, B. C., Burks, A., Gross, R. E., Inman, C. S., Jobst, B. C., Goren-  
424 stein, M. A., Davis, K. A., Worrell, G. A., Kucewicz, M. T., Stein, J. M., Gorniak, R.,  
425 Das, S. R., Rizzuto, D. S., and Kahana, M. J. (2018). Closed-loop stimulation of tem-  
426 poral cortex rescues functional networks and improves memory. *Nature Communications*,  
427 9(365):<https://doi.org/10.1038/s41467-017-02753-0>.
- 428 [9] Finn, E. S., Shen, X., Scheinost, D., Rosenberg, M. D., Huang, J., Chun, M. M., Papademetris,  
429 X., and Constable, R. T. (2015). Functional connectome fingerprinting: identifying individuals  
430 using patterns of brain connectivity. *Nature Neuroscience*, 18:1664 – 1671.
- 431 [10] Grabner, G., Janke, A. L., Budge, M. M., Smith, D., Pruessner, J., and Collins, D. L. (2006).  
432 Symmetric atlasing and model based segmentation: an application to the hippocampus in  
433 older adults. *Medical Image Computing and Computer-Assistend Intervention*, 9:58–66.
- 434 [11] Hillebrand, A., Singh, K. D., Holliday, I. E., Furlong, P. L., and Barnes, G. R. (2005). A new  
435 approach to neuroimaging with magnetoencephalography. *Human Brain Mapping*, 25:199–  
436 211.

- 437 [12] Horak, P. C., Meisenhelter, S., Song, Y., Testorf, M. E., Kahana, M. J., Viles, W. D., Bujarski,  
438 K. A., Connolly, A. C., Robbins, A. A., Sperling, M. R., Sharan, A. D., Worrell, G. A., Miller,  
439 L. R., Gross, R. E., Davis, K. A., Roberts, D. W., Lega, B., Sheth, S. A., Zaghloul, K. A., Stein,  
440 J. M., Das, S. R., Rizzuto, D. S., and Jobst, B. C. (2017). Interictal epileptiform discharges  
441 impair word recall in multiple brain areas. *Epilepsia*, 58(3):373–380.
- 442 [13] Huster, R. J., Debener, S., Eichele, T., and Herrmann, C. S. (2012). Methods for simultaneous  
443 EEG-fMRI: an introductory review. *The Journal of Neuroscience*, 32(18):6053–6060.
- 444 [14] Jacobs, J., Kahana, M. J., Ekstrom, A. D., Mollison, M. V., and Fried, I. (2010). A sense of  
445 direction in human entorhinal cortex. *Proceedings of the National Academy of Sciences, USA*,  
446 107(14):6487–6482.
- 447 [15] Jahanshad, N., Kochunov, P. V., Sprooten, E., Mandl, R. C., Nichols, T. E., Almasy, L.,  
448 Blangero, J., Brouwer, R. M., Curran, J. E., de Zubicaray, G. I., Duggirala, R., Fox, P. T., Hong,  
449 L. E., Landman, B. A., Martin, N. G., McMahon, K. L., Medland, S. E., Mitchell, B. D., Olvera,  
450 R. L., Peterson, C. P., Starr, J. M., Sussmann, J. E., Toga, A. W., Wardlaw, J. M., Wright, M. J.,  
451 Pol, H. E. H., Pastin, M. E., McIntosh, A. M., Deary, I. J., Thompson, P. M., and Glahn, D. C.  
452 (2013). Multi-site genetic analysis of diffusion images and voxelwise heritability analysis: A  
453 pilot project of the enigma-dti working group. *NeuroImage*, 81(1):455–469.
- 454 [16] Kragel, J. E., Ezzyat, Y., Sperling, M. R., Gorniak, R., Worrell, G. A., Berry, B. M., Inman,  
455 C., Lin, J.-J., Davis, K. A., Das, S. R., Stein, J. M., Jobst, B. C., Zaghloul, K. A., Sheth, S. A.,  
456 Rizzuto, D. S., and Kahana, M. J. (2017). Similar patterns of neural activity predict memory  
457 formation during encoding and retrieval. *NeuroImage*, 155:70–71.
- 458 [17] Kucewicz, M. T., Berry, B. M., Kremen, V., Brinkmann, B. H., Sperling, M. R., Jobst, B. C.,  
459 Gross, R. E., Lega, B., Sheth, S. A., Stein, J. M., Das, S. R., Gorniak, R., Stead, S. M., Rizzuto,

- 460 D. S., Kahana, M. J., and Worrell, G. A. (2017). Dissecting gamma frequency activity during  
461 human memory processing. *Brain*, 140:1337–1350.
- 462 [18] Kucewicz, M. T., Berry, B. M., Miller, L. R., Khadjevand, F., Ezzyat, Y., Stein, J. M., Kremen,  
463 V., Brinkmann, B. H., Wanda, P., Sperling, M. R., Gorniak, R., Davis, K. A., Jobst, B. C., Gross,  
464 R. E., Lega, B., Gompel, J. V., Stead, S. M., Rizzuto, D. S., Kahana, M. J., and Worrell, G. A.  
465 (2018). Evidence for verbal memory enhancement with electrical brain stimulation in the  
466 lateral temporal cortex. *Brain*, 141(4):971–978.
- 467 [19] Lin, J.-J., Rugg, M. D., Das, S., Stein, J., Rizzuto, D. S., Kahana, M. J., and Lega, B. C.  
468 (2017). Theta band power increases in the posterior hippocampus predict successful episodic  
469 memory encoding in humans. *Hippocampus*, 27:1040–1053.
- 470 [20] Manning, J. R., Jacobs, J., Fried, I., and Kahana, M. J. (2009). Broadband shifts in LFP power  
471 spectra are correlated with single-neuron spiking in humans. *The Journal of Neuroscience*,  
472 29(43):13613–13620.
- 473 [21] Manning, J. R., Polyn, S. M., Baltuch, G., Litt, B., and Kahana, M. J. (2011). Oscillatory  
474 patterns in temporal lobe reveal context reinstatement during memory search. *Proceedings of  
475 the National Academy of Sciences, USA*, 108(31):12893–12897.
- 476 [22] Manning, J. R., Ranganath, R., Norman, K. A., and Blei, D. M. (2014). Topographic  
477 factor analysis: a Bayesian model for inferring brain networks from neural data. *PLoS One*,  
478 9(5):e94914.
- 479 [23] Manning, J. R., Sperling, M. R., Sharan, A., Rosenberg, E. A., and Kahana, M. J. (2012).  
480 Spontaneously reactivated patterns in frontal and temporal lobe predict semantic clustering  
481 during memory search. *The Journal of Neuroscience*, 32(26):8871–8878.

- 482 [24] Manning, J. R., Zhu, X., Willke, T. L., Ranganath, R., Stachenfeld, K., Hasson, U., Blei,  
483 D. M., and Norman, K. A. (2018). A probabilistic approach to discovering dynamic full-brain  
484 functional connectivity patterns. *NeuroImage*.
- 485 [25] Miller, K. J., Shenoy, P., den Nijs, M., Sorensen, L. B., Rao, R. P. N., and Ojemann, J. G. (2008).  
486 Beyond the gamma band: the role of high-frequency features in movement classification.  
487 *IEEE Transactions on Biomedical Engineering*, 55(5):1634 – 1637.
- 488 [26] Mori, S., Oishi, K., Jiang, H., Jiang, L., Li, X., Akhter, K., Hua, K., Faria, A. V., Mahmood,  
489 A., Woods, R., Toga, A. W., Pike, G. B., Neto, P. R., Evans, A., Zhang, J., Huang, H., Miller,  
490 M. I., van Zijl, P., and Mazziotta, J. (2008). Stereotaxic white matter atlas based on diffusion  
491 tensor imaging in an icbm template. *NeuroImage*, 40(2):570–582.
- 492 [27] Rasmussen, C. E. (2006). *Gaussian processes for machine learning*. MIT Press.
- 493 [28] Sarvas, J. (1987). Basic mathematical and electromagnetic concepts of the biomagnetic  
494 inverse problem. *Phys. Med. Biol.*, 32(1):11–22.
- 495 [29] Sawyer, R. J. (1995). *The Terminal Experiment*. HarperPrism.
- 496 [30] Sederberg, P. B., Kahana, M. J., Howard, M. W., Donner, E. J., and Madsen, J. R. (2003). Theta  
497 and gamma oscillations during encoding predict subsequent recall. *Journal of Neuroscience*,  
498 23(34):10809–10814.
- 499 [31] Sederberg, P. B., Schulze-Bonhage, A., Madsen, J. R., Bromfield, E. B., Litt, B., Brandt,  
500 A., and Kahana, M. J. (2007a). Gamma oscillations distinguish true from false memories.  
501 *Psychological Science*, 18(11):927–932.
- 502 [32] Sederberg, P. B., Schulze-Bonhage, A., Madsen, J. R., Bromfield, E. B., McCarthy, D. C.,  
503 Brandt, A., Tully, M. S., and Kahana, M. J. (2007b). Hippocampal and neocortical gamma  
504 oscillations predict memory formation in humans. *Cerebral Cortex*, 17(5):1190–1196.

- 505 [33] Sejnowski, T. J., Churchland, P. S., and Movshon, J. A. (2014). Putting big data to good use  
506 in neuroscience. *Nature Neuroscience*, 17:1440–1441.
- 507 [34] Snyder, A. Z. (1991). Dipole source localization in the study of EP generators: a critique.  
508 *Electroencephalography and Clinical Neurophysiology*, 80(4):321–325.
- 509 [35] Solomon, E. A., Gross, R., Lega, B., Sperling, M. R., Worrell, G., Sheth, S. A., Zaghloul,  
510 K. A., Jobst, B. C., Stein, J. M., Das, S., Gorniak, R., Inman, C., Seger, S., Kragel, J. E., Rizzuto,  
511 D. S., and Kahana, M. J. (2018). Mtl functional connectivity predicts stimulation-induced  
512 theta power. *Nature Communications*, In press.
- 513 [36] Sporns, O. and Betzel, R. F. (2016). Modular brain networks. *Annual Review of Psychology*,  
514 67:613–640.
- 515 [37] Talairach, J. and Tournoux, P. (1988). *Co-planar stereotaxic atlas of the human brain*. Verlag,  
516 Stuttgart.
- 517 [38] Tavor, I., Jones, O. P., Mars, R. B., Smith, S. M., Behrens, T. E., and Jbabdi, S. (2016). Task-  
518 free MRI predicts individual differences in brain activity during task performance. *Science*,  
519 352(6282):216–220.
- 520 [39] Turk-Browne, N. B. (2013). Functional interactions as big data in the human brain. *Science*,  
521 342:580–584.
- 522 [40] Weidemann, C. T., Kragel, J. E., Lega, B. C., Worrell, G. A., Sperling, M. R., Sharan, A. D.,  
523 Jobst, B. C., Khadjevand, F., Davis, K. A., Wanda, P. A., Kadel, A., Rizzuto, D. S., and Kahana,  
524 M. J. (2018). Neural activity reveals interactions between episodic and semantic memory  
525 systems during retrieval. *Journal of Experimental Psychology: General*, In press.
- 526 [41] Yeo, B. T. T., Krienen, F. M., Sepulcre, J., Sabuncu, M. R., Lashkari, D., Hollinshead, M.,  
527 Roffman, J. L., Smoller, J. W., Zollei, L., Polimieni, J. R., Fischl, B., Liu, H., and Buckner,

- 528 R. L. (2011). The organization of the human cerebral cortex estimated by intrinsic functional
- 529 connectivity. *Journal of Neurophysiology*, 106(3):1125–1165.